Software framework and method for the alignment of the LHCb RICH optical system using proton-proton collisions during LHC Run II

XXX[1].

[1] *University of Bristol, Bristol, United Kingdom*

Abstract

The method for aligning the optical system of the LHCb Ring-Imaging Cherenkov (RICH) detectors during Run II of the Large Hadron Collider (LHC) is presented. The alignment will run online, within the high performance trigger system, and will be performed for each LHC fill. The alignment method for the RICH detectors is outlined, as well as its implementation in a novel online framework. The performance and stability of the alignments over the 2015 data taking period is shown.

1 Introduction

The LHCb experiment uses two ring-imaging Cherenkov (RICH) detectors to provide powerful discrimination between charged particles in the intense hadron production environment of the LHC. These two separate RICH detectors have different radiators and are designed to provide particle identification over a momentum range of 1 to 100 GeV/c [1]. The performance of the particle identification supplied by the RICH system [2] strongly depends on the quality of its alignment, i.e. how accurately the physical position of each component of the RICH detectors is described in the LHCb software. The goal of the alignment procedure is determine the exact position of all optical components and propagate this information to the LHCb conditions database that stores the non-event time-varying data pertaining to detector conditions.

The LHCb detector achieved excellent performance in Run I but faces more challenging conditions in Run II. The LHC will collide protons at an increased centre-of-mass energy of 13 TeV and with 25 ns bunch spacing. The spatial alignment of the detector and the accurate calibration of its subcomponents are essential to achieve the best physics performance. In order to keep the selection efficiencies in the high level trigger as high as in Run I, conditions on the particle identification will be used in Run II. This requires the full alignment and calibration of the RICH detectors within the high performance trigger sequence.

This note describes how the LHCb RICH optical systems are aligned in software in Run II using proton-proton collision data. The method used is discussed in Sec. 3, while the computing framework and the implementation for the automated running of the alignment is described in Sec. 4. The results for the data-taking period in 2015 are presented in Section **??**.

$$O = \frac{\sum^{ADC>thresh.} N_{events}}{\sum N_{events}} \tag{1}$$

2 The LHCb detector

The LHCb detector [1, 3] is a single-arm forward spectrometer covering the pseudorapidity range $2 < \eta < 5$, designed for the study of particles containing b or c quarks. The detector includes a high-precision tracking system consisting of a silicon-strip vertex detector surrounding the pp interaction region, a large-area silicon-strip detector located upstream of a dipole magnet with a bending power of about 4 Tm, and three stations of silicon-strip detectors and straw drift tubes placed downstream of the magnet. The tracking system provides a measurement of momentum, p, of charged particles with a relative uncertainty that varies from 0.5% at low momentum to 1.0% at 200 GeV/c. The minimum distance of a track to a primary vertex, the impact parameter, is measured with a resolution of $(15 + 29/p_{\mathrm{T}})$ μm, where p_{T} is the component of the momentum transverse to the beam, in GeV/c.

Different types of charged hadrons are distinguished using information from two ring-imaging Cherenkov detectors [2]. Photons, electrons and hadrons are identified by a calorimeter system consisting of scintillating-pad and preshower detectors, an electromagnetic calorimeter and a hadronic calorimeter. Muons are identified by a system composed of alternating layers of iron and multiwire proportional chambers.

The event selection is performed by a trigger, which consists of a hardware stage, based on information from the calorimeter and muon systems, followed by a software stage, which applies a full event reconstruction.

In Run II, the alignment and calibration of all subdetectors is performed online in between different stages of the high level trigger (HLT) and the results are immediately applied to the reconstruction.

2.1 RICH optical systems

Both RICH1 and RICH2 have two sets of mirrors: the primary spherical mirrors, and the secondary (a.k.a. plane, flat), much flatter mirrors. Cherenkov photons emitted by a charged track are reflected off a primary mirror onto a secondary mirror, and from there out of the LHCb acceptance onto the plane of photon detectors, which coincides with the focal plane of the given part of the optical systems. The RICH1/RICH2 optical systems consists of 4/56 primary and 16/40 secondary mirrors. The layouts of the RICH optical systems are shown in Figure 1 [4, 5], while the structures of the mirror arrays and their numbering are shown in Figures 5 and 6 of Section 3.

The right-handed coordinate system of each mirror segment is defined by placing the origin at the centre of curvature with the x-axis pointing towards the mirror, the y-axis pointing upwards and the corresponding z-axis being horizontal. Finally, the pivot point for the software rotations around the y- and z-axes is at the centre of each mirror.

In order to achieve the optimal performance of the LHCb RICH detector we aim to minimize the uncertainty, σ, associated with the measurement of a single photon Cherenkov angle. This is limited by four main sources of uncertainty outlined in Table 1.

Adding them in quadrature gives the minimal total uncertainty, which can be obtained by having an optimal alignment of all optical components of the RICH detectors.

Table 1: Sources of uncertainty, σ, of the measurement of a single photon Cherenkov angle for the three LHCb RICH radiators.

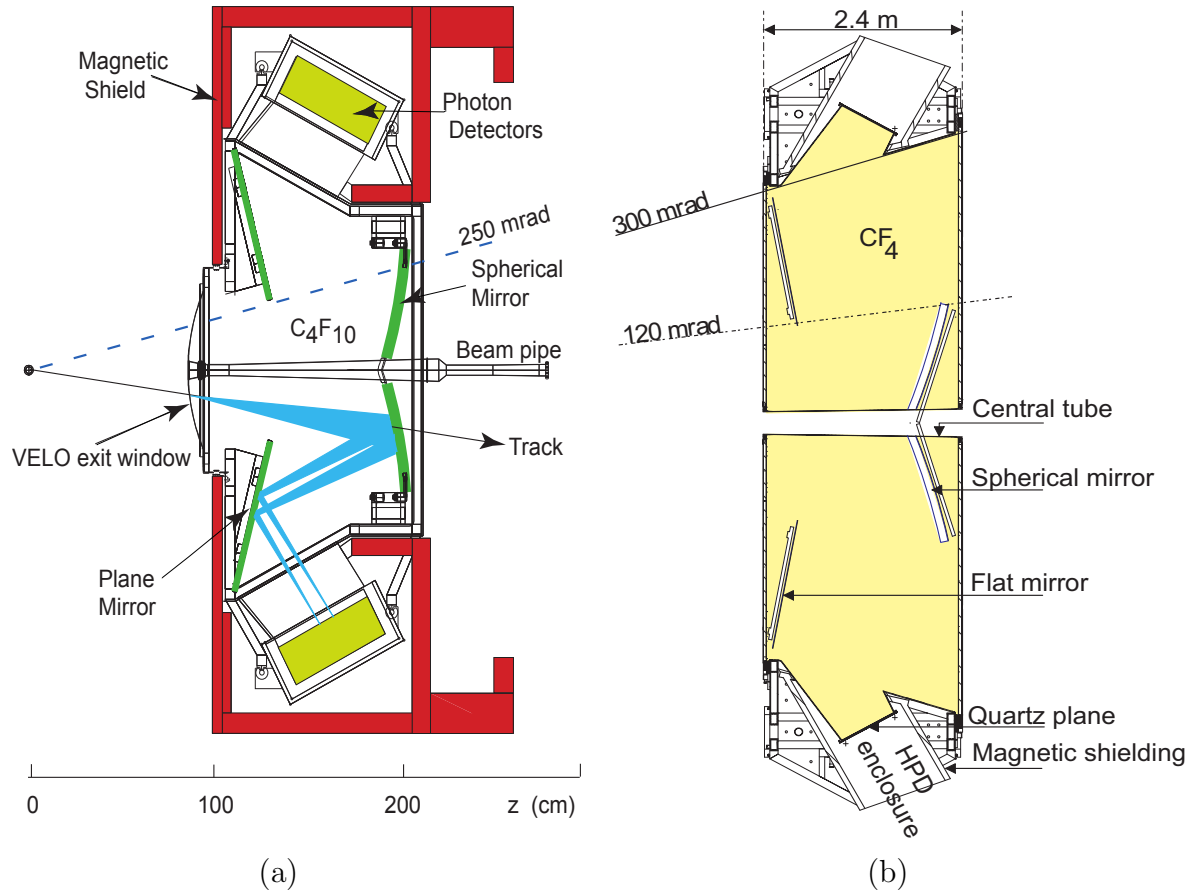|	σ [mrad]	
	RICH1	RICH2
	C_4F_{10}	CF_4
Emission point	0.8	0.2
Chromatic dispersion	0.9	0.5
Pixel size	0.6	0.2
Tracking	0.4	0.4
Total	1.5	0.7

Figure 1: Schematic view of the LHCb RICH detectors and their optical systems: (a) side view of RICH1 and (b) top view of RICH2. Formation of a Cherenkov ring in the lower part of RICH1 is also drawn.

3 Method of alignment for the RICH optical system

Photons are "reconstructed" from hits on the photon detector plane by reflecting them off the RICH mirrors, based on the RICH geometry information available to the LHCb reconstruction software. For definiteness, the photons are assumed to originate from the midpoint of a track as it traverses the RICH radiator. This assumption allows a Cherenkov angle to be calculated.

A misalignment of the LHCb RICH optical system manifests itself as a displacement of the observable Cherenkov ring against the expected one [6, 7]. In other words, a discrepancy occurs between the actual centre of the Cherenkov ring and its expected position calculated from the reconstructed tracks momentum and using pion mass hypothesis. This is explained in Fig. 2 and its caption (partly inspired by the respective figure from [8]).

A method of finding appropriate software compensations for the mirror misalign-
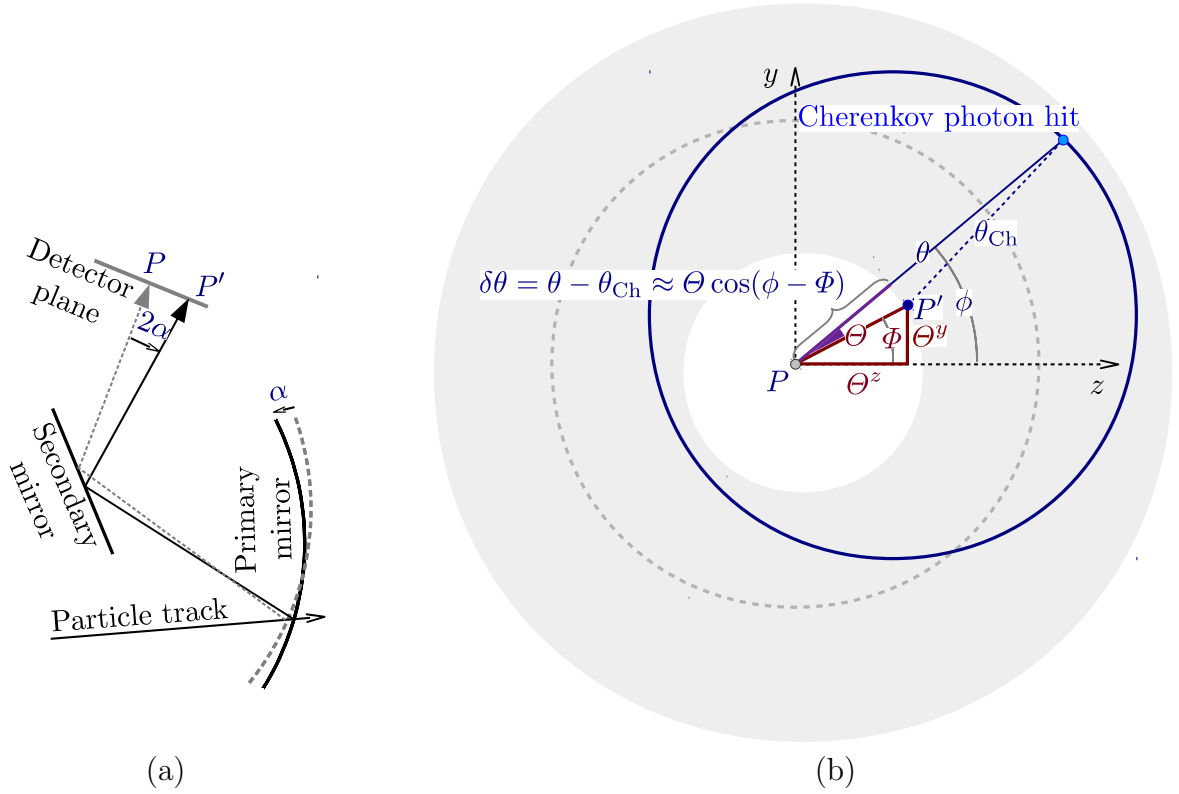
3

Figure 2: (a) Schematic drawing of how rotational misalignment of a RICH mirror (primary mirror in this example) causes shift of the actual centre P' of the Cherenkov ring on the photon detector plane. The "reflection" of the track is drawn only for explanatory purpose. (b) The expected Cherenkov angle θ_{Ch} and the reconstructed Cherenkov angle θ are displayed shifted by Θ^z and Θ^y. P marks the position of the extrapolated track projection calculated without adjustments that would compensate misalignment of the mirrors, while P' is the actual (unknown) position of the centre of the ring. Cherenkov angles θ are evaluated relative to P, and therefore, vary with ϕ. The gray stripe represents area around the expected ring from which the photon hits are "reconstructed". Obviously, the width of this stripe is empirically chosen wide enough to cover the actual shifted (and somewhat smeared) ring of hits from the given track. Inevitably, the "noise" background photon hits in this area are also "reconstructed"

ments by the use of data was developed in the HERAb experiment [8]. The approach presented here builds on that method and is developed further to address a more complex design of the LHCb RICH system. In each half of the HERAb optical system 40 primary mirrors form an ample number of efficient same-photon reflecting combinations with 18 secondary mirrors [9], while in each half of the LHCb RICH2 sub-detector, 28 primary mirrors reflect photons onto 20 secondary mirrors. Therefore, effectively, the ratio of the number of useful mirror combinations (for building a consistent system of equations) to the number of mirror segments (and hence unknowns) is lower.
A displacement of the actual position of the Cherenkov ring centre from the computed position of the corresponding track projection can be observed by plotting $\delta\theta$ against

the azimuthal angle ϕ around the ring

$$\delta\theta\left(\phi\right) = \theta\left(\phi\right) - \theta_{\mathrm{Ch}},$$

where θ_{Ch} is the Cherenkov angle of a photon (Equation **??**) that hit circular stripe of a certain width around the expected ring (see Fig. 2 (b)). We select only high-momentum tracks: in this limit the mass difference between pions and kaons becomes insignificant and the Cherenkov angle is said to reach saturation. At saturation all particles tend to the same value of θ_{Ch}. We can approximate all particles to be pions, thus the mass, m, is assumed to be that of a charged pion. Figure 3 illustrates the saturation of θ_{Ch} in the RICH1 gaseous radiator. For an aligned system position the mode of the $\delta\theta$ distribution
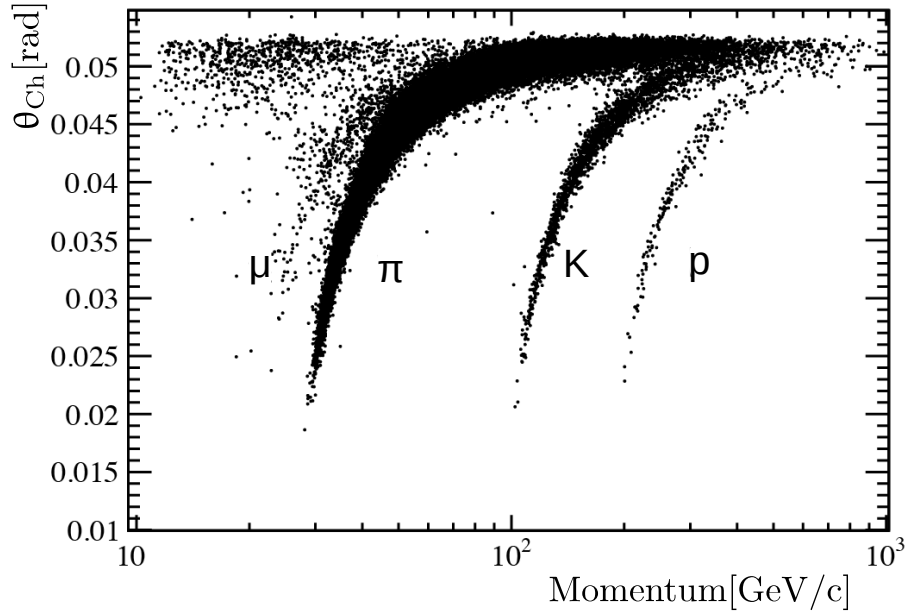

Figure 3: Cherenkov angle θ_{Ch} against track momentum, for tracks traversing the RICH1 gaseous radiator. Muons, pions, kaons and protons are visible. As the track momentum increases, all particles tend towards the same θ_{Ch}, known as the saturated Cherenkov angle.

is constant with ϕ for any mirror combination. It can be seen from Fig. 2 (b), that any small misalignment results in an approximately sinusoidal dependence of the mode of the $\delta\theta$ vs. ϕ distribution (described by Equation 2).
Theoretically, to associate a "Cherenkov angle" with a photon hit on the photodetector plane, we need to "reconstruct" the photon, i.e. to appropriately connect its point of emission, via two reflections, with the given hit. The point of emission is certainly known only in MC. Because a photon emitted from any point along the track (at the given ϕ) will ideally hit the same spot on the photodetector plane, in the case of data the emission point should be chosen voluntarily. Analysis of MC events has shown [8] that to reduce noise from the photons falsely associated with a given track, only "unambiguous" hits should be chosen. An "unambiguous" hit yields reflection of the corresponding hypothetical photon off the same combination of mirrors even if assumed to be emitted at the beginning and at the end of the track path in the radiator. In our analysis we use "unambiguous" photons.

Our aim is to detect any extra rotations of all mirror segments, both primary and secondary, around z and y axes against their position descriptions contained in the Detector Description Database (DDDB) that had been already corrected with the up-to-this-time misalignment corrections contained in the Conditions Database (CONDDB). Traditionally, all distances (displacements) on the photodetector plane are expressed in terms of the polar angle θ, which is approximately correct, because optical paths for photons from the surface of a primary mirror to their hits in the vicinity of the respective ring on the photodetector plane (for the corresponding track and particular mirror combination, of course) are almost the same.

As follows from Fig. 2, if one or both of a combination of primary mirror p and secondary mirror s are misaligned, the measured Cherenkov angle depends on ϕ, and the difference between measured and expected values looks like

$$
\begin{aligned}
\delta\theta_{p,s}(\phi) \equiv [\theta(\phi) - \theta_{\mathrm{Ch}}]_{p,s} &\approx [\Theta\cos(\phi - \Phi)]_{p,s} \\
&= [\Theta\cos\Phi\cos\phi + \Theta\sin\Phi\sin\phi]_{p,s} \\
&= \Theta^z_{p,s}\cos\phi + \Theta^y_{p,s}\sin\phi
\end{aligned}
\tag{2}
$$

where $\Theta^z_{p,s}$ and $\Theta^y_{p,s}$ are combined tilts around respective axes, resulting from tilts of both mirrors of the combination. On the other hand, they are equal to the sum of those tilts taken with the so-called "magnification factors". Namely, the resulting displacement components of a ring of photons reflected off a combination of primary mirror p and secondary mirror s, that are rotated by angles α^y_p, α^z_p, β^y_s and β^z_s, respectively, are

$$
\begin{aligned}
A^y_{p,s}\alpha^y_p + B^y_{p,s}\beta^y_s + a^y_{p,s}\alpha^z_p + b^y_{p,s}\beta^z_s = \Theta^y_{p,s} \\
A^z_{p,s}\alpha^z_p + B^z_{p,s}\beta^z_s + a^z_{p,s}\alpha^y_p + b^z_{p,s}\beta^y_s = \Theta^z_{p,s}
\end{aligned}
\tag{3}
$$

where $A^y_{p,s}$, $B^y_{p,s}$, $a^y_{p,s}$ and $b^y_{p,s}$ ($A^z_{p,s}$, $B^z_{p,s}$, $a^z_{p,s}$ and $b^z_{p,s}$ for the z-axis) are the corresponding magnification factors, discussed in the next section.

To correct for the mirror misalignments, the projected combined mirror misalignment onto the photodetector plane, $\Theta^y_{p,s}$ and $\Theta^z_{p,s}$ in Fig. 2, are determined for each mirror combination from a subset of all possible mirror combinations sufficient for determining misalignments of every mirror. This is achieved by plotting $\delta\theta(\phi)_{p,s}$ and fitting it by a sinusoidal function (see Equation 2) as described in Sec. 3.3. This misalignment is decomposed into a combination of individual primary and/or secondary mirror rotational misalignments, as described in Sec. 3.4, by solving a system of linear equations, similar to Equations 3. We correct for the misalignment by applying corresponding compensating rotations to the mirrors. This procedure is repeated until all the calculated remaining misalignments, α^y_p, α^z_p, β^y_s and β^z_s, are less than 0.1 mrad.

3.1 Magnification factors

To understand the origin of the magnification factors, let us consider in more detail (although in simplified manner) how tilts of mirror segments affect displacement of the Cherenkov ring against its expected position. For example, small rotations of primary

and secondary mirrors around their vertical (y) axes yield approximately the following displacement of the ring in terms of distance (note that rotation of a mirror by e.g. α^y, results in deflecting photons by $2\,\alpha^y$ in horizontal plane, as shown in Fig. 2):

$$l\,\Theta^y \approx l_{\text{pri}}2\,\alpha^y - l_{\text{sec}}2\,\beta^y,$$

where l, l_{pri} and l_{sec} are paths of the photons to the photodetectors (total, from primary, and from secondary mirrors, respectively). Or in terms of Cherenkov angles

$$\Theta^y \approx \frac{2\,l_{\text{pri}}}{l}\alpha^y - \frac{2\,l_{\text{sec}}}{l}\beta^y \approx A^y\alpha^y + B^y\beta^y.$$

Similarly, for small rotations around horizontal axes

$$\Theta^z \approx \frac{2\,l_{\text{pri}}}{l}\alpha^z + \frac{2\,l_{\text{sec}}}{l}\beta^z \approx A^z\alpha^z + B^z\beta^z.$$

For each mirror combination the magnification factors are evaluated by introducing 8 independent calibrational rotations (positive or negative rotations about the $y-$ or $z-$axes for the primary or secondary mirrors) and by measuring the resulting total tilts. In particular, ± 0.3 mrad rotations are used. That choice is motivated by the fact that typically, Cherenkov angle resolution, the half-width of the θ distribution, for RICH2 is around 0.7 mrad. The final value of each factor is arithmetical mean of the two corresponding values obtained with the calibrating rotations in opposite directions. Although naïvely we would expect $l = l_{\text{pri}}$, in practice, due to complicated averaging of the "reconstructed" photon paths for every mirror combination, the factors have somewhat differing values, and on average look approximately like

$$\Theta^y \approx 2.0\,\alpha^y - 0.9\,\beta^y \ \text{ and } \ \Theta^z \approx 1.8\,\alpha^z + 0.6\,\beta^z.$$

In reality, there is also a small but still significant cross-influence between rotations around alternative axes: e.g. rotation of a mirror around y-axis yields also a small deflection of the photon in the perpendicular plane, i.e. around z-axis. That is why Equations 3 contain also the corresponding cross-terms. As for the cross-term magnification factors, a^y, b^y, a^z and b^z, their absolute values vary approximately between 0.001 and 0.250, and they can be positive as well as negative.

3.2   Alignment parameters

A list of alignment parameters is shown in Table 2. The table outlines the parameters which are observable and those that need to be found and corrected for in the alignment process. Note that the magnification factors are not known in advance and need to be found as well, as was discussed in Sec. 3.1.

7

Table 2: Alignment parameters.

Parameter	Definition
p	primary mirror number: 0-3 for RICH1, 0-55 for RICH2
s	secondary mirror number: 0-15 for RICH1, 0-39 for RICH2
$\Theta_{p,s}^{y}/\Theta_{p,s}^{z}$	observed combined misalignment on the photo-detector plane in the y-axis/z-axis, for mirror combination (p,s)
$\alpha_{p}^{y}/\alpha_{p}^{z}$	calculated misalignment of primary mirror p as a tilt about its local y-axis/z-axis
$\beta_{s}^{y}/\beta_{s}^{z}$	calculated misalignment of secondary mirror s as a tilt about its local y-axis/z-axis
$A_{p,s}^{y}/A_{p,s}^{z}$	magnification factor to map $\alpha_{p}^{y}/\alpha_{p}^{z}$ onto $\Theta_{p,s}^{y}/\Theta_{p,s}^{z}$ (tilts resulting from rotations around the same axes)
$B_{p,s}^{y}/B_{p,s}^{z}$	magnification factor to map $\beta_{s}^{y}/\beta_{s}^{z}$ onto $\Theta_{p,s}^{y}/\Theta_{p,s}^{z}$ (tilts resulting from rotations around the same axes)
$a_{p,s}^{y}/a_{p,s}^{z}$	magnification factor to map $\alpha_{p}^{z}/\alpha_{p}^{y}$ onto $\Theta_{p,s}^{y}/\Theta_{p,s}^{z}$ (minor tilts resulting from rotations around the alternative axes)
$b_{p,s}^{y}/b_{p,s}^{z}$	magnification factor to map $\beta_{s}^{z}/\beta_{s}^{y}$ onto $\Theta_{p,s}^{y}/\Theta_{p,s}^{z}$ (minor tilts resulting from rotations around the alternative axes)

3.3 Fitting method

For every chosen combination of primary mirror p and secondary mirror s, $\delta\theta$ is plotted against ϕ. Each of these histograms is divided into 20 bins in ϕ. Inside each ϕ bin the $\delta\theta$ distribution is fitted with a Gaussian plus first/second order (for RICH1/RICH2) polynomial background. In accordance with Equation 2 the ϕ dependence of the position of the Gaussian peak for a given mirror combination (p,s) is approximated by

$$\delta\theta_{p,s}(\phi) = \Theta_{p,s}^{z} \cos\phi + \Theta_{p,s}^{y} \sin\phi. \tag{4}$$

Equation 4 is used as a bond when fitting all the 20 slices jointly. The fitting is done by means of the ROOT framework [10], in particular, using the MINUIT 2 minimization package. The values of the fitted parameters $\Theta_{p,s}^{y}$ and $\Theta_{p,s}^{z}$ correspond to misalignment of that mirror combination mapped to apparent displacement of the ring on the photo-detector plane, as explained in Fig. 2. An example of such a fit for misaligned mirror combination $(0,1)$ of RICH1 is shown in Fig. 4: before alignment (left), and after alignment (right).

3.4 Determining individual mirror misalignments

If we can map a measured Cherenkov ring misalignment to individual mirror rotations, we can compensate for it in the software. Obviously, there is no straightforward way to do that. However, optimal alignment can be achieved if each component of the optical
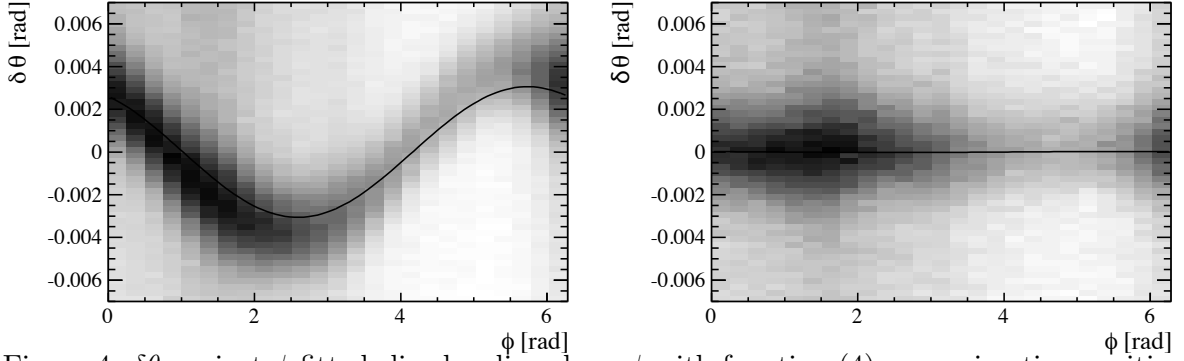
Figure 4: $\delta\theta$ against ϕ fitted slice-by-slice along ϕ with function (4) approximating position of the Gaussian peak on the ϕ-$\delta\theta$ plane for combination of primary mirror 0 and secondary mirror 1 of RICH1 detector. The originally misaligned mirror combination is represented on the left. On the right — same fit after the combination is aligned.

system is properly aligned relative to all others. In this sense finding the absolute alignment of each individual component is not significantly important. We therefore aim to align all mirrors relative to each other.

3.4.1 RICH1 alignment

The geometry of the LHCb RICH1 detector restricts the number of populated mirror combinations to 16, Fig. 5. Photons reflected off a primary mirror are then reflected off one of four secondary mirrors that form a group, unique to that primary mirror. Each of the four quadrants contain a single primary mirror and four secondary mirrors. The misalignments of the four mirror combinations in each quadrant are determined using the method discussed in Sec. 3.3.
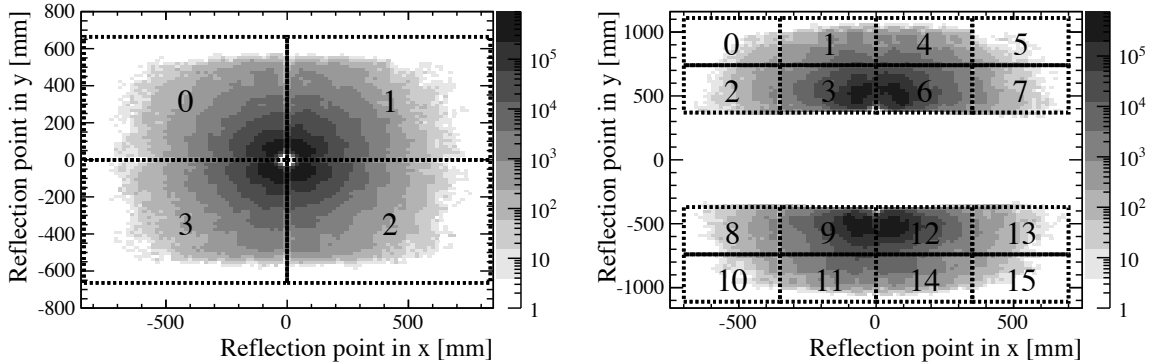

Figure 5: Reflection point distribution of photons off RICH1 primary mirrors (left) and secondary mirrors (right). The photon population across mirrors is not uniform with the higher populated mirrors laying closest to the beam-pipe. Also shown is the RICH1 mirror numbering schema, viewed along the beam.

Thus, e.g. for quadrant 0 in the y-direction, we have four equations for five unknowns

200 $(\alpha_0^y, \beta_0^y, \ldots, \beta_3^y)$

$$A_{0,0}^y \alpha_0^y + B_{0,0}^y \beta_0^y = \Theta_{0,0}^y$$
$$\vdots \qquad \vdots \qquad \vdots$$
$$A_{0,3}^y \alpha_0^y + B_{0,3}^y \beta_3^y = \Theta_{0,3}^y.$$

201 One option is to exclude the primary mirror from the adjustment procedure, i.e. set
202 $\alpha_0^y = 0$, and then directly calculate misalignments of each secondary mirror: $\beta_s^y =$
203 $\Theta_{0,s}^y / B_{0,s}^y$.
204 Instead, we first attempt to align the primary mirrors. For each quadrant, we tempor-
205 arily neglect misalignments of the secondary mirrors, i.e. set $\beta_s^y = 0$, calculate four
206 misalignment estimates $(\alpha_p^y)_s = \Theta_{p,s}^y / A_{p,s}^y$ for the primary mirror (in conjunction with
207 the four different secondary mirrors s) and their average

$$\alpha_p^y = \frac{1}{4} \sum_s (\alpha_p^y)_s$$

208 becomes an estimate of misalignment of that primary mirror. It is then used to find the
209 misalignment of each secondary mirror of that quadrant:

$$\beta_s^y = \frac{\left(\Theta_{p,s}^y - A_{p,s}^y \alpha_p^y\right)}{B_{p,s}^y}.$$

210 The final effect of the misalignment compensation is the same as in case of the first op-
211 tion, although the individual mirror adjustments are different. All the obtained adjust-
212 ments are then inserted into the software. The same is done for misalignments around
213 the z-axis.
214 Because the magnification factors become slightly altered after the mirror adjustment,
215 we are unable to find the final solution of the system of equations in one pass. There-
216 fore, we iterate over the same data — re-evaluating the total tilts produced by each
217 combination and the respective magnification factors using the updated compensa-
218 tions — until the calculated remaining misalignments, α_p^y, α_p^z, β_s^y and β_s^z, are less than
219 0.1 mrad.

3.4.2 RICH2 alignment

221 The geometrical layout of the RICH2 detector is significantly different to that of
222 RICH1, and therefore we cannot find the mirror misalignments with the same method.
223 The RICH2 detector has 56 primary (mostly hexagonal) and 40 secondary (rectangular)
224 mirror segments. Each hexagonal segment can be inscribed in a circle of a radius of
225 $r_{\mathrm{m}} = 251$ mm. The maximum base radius of the Cherenkov cones on the primary mir-
226 rors is $r_{\mathrm{Ch}} = 55$ mm, therefore probability of having a ring imaged by only one primary
227 mirror segment is $p_{\mathrm{Ch}} \approx 1 - r_{\mathrm{Ch}}/r_{\mathrm{m}} \approx 78\%$, which makes easier pattern recognition and
228 correction in case of mirror misalignments [11].
229 All mirrors are divided into two decoupled systems: 48 on the left of the beam, and 48
230 on the right of the beam. This gives 96 unknown parameters for each side (tilts around
231 y and z axes for each mirror). Their numbering schema is shown in Fig. 6
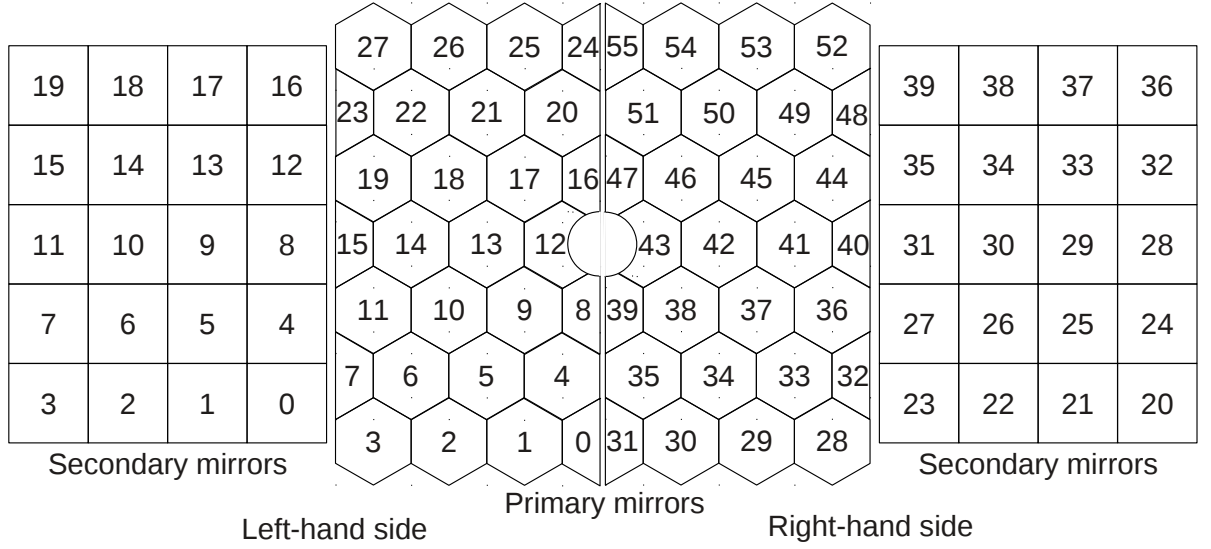
Figure 6: RICH2 mirror segmentation and the numbering schema, viewed along the beam. The beampipe is at the centre.

However, only 47 out of 48 possible tilts around each axis are independent, because if we simultaneously rotate all primary mirrors by one angle and all secondary mirrors by the corresponding angle in the opposite direction, the ring position will not change.

Table 4: Chosen 47 p, s (primary,secondary) mirror combinations grouped by primary mirror numbers (left-hand side of RICH2).

27,19		26,18		25,17		24,16
	22,19	22,18		21,17		20,16
23,15		22,14		21,13		20,12
19,15		18,14		17,13		16,12
19,11		18,10		17,9		16,8
15,11	14,11	14,10	13,10	13,9	12,9	12,8
11,11		10,10		9,9		8,8
11,7		10,6		9,5		8,4
7,7		6,6		5,5		4,4
	6,3	6,2		5,1		4,0
3,3		2,2		1,1		0,0

Tables 4 and 5 and Fig. 7 – each in its own way – present the set of combinations chosen for the alignment procedure. The goal is to have consistent system of equations for determining the individual misalignments. In particular, it is seen, that almost each primary mirror is combined with at least two secondary mirrors. Overall, useful mirror combinations are selected such that all mirrors are linked together. By fixing the misalignment of one of the primary mirrors (12) we find the misalignment of the secondary mirror with which it forms a combination. This secondary mirror also forms combination with another primary mirror which allows to find its misalignment in turn. This

11

Table 5: Chosen 47 p, s (primary,secondary) mirror combinations grouped by secondary mirror numbers (left-hand side of RICH2).

	27,19		26,18		25,17	24,16
	22,19		22,18		21,17	20,16
	23,15		22,14		21,13	20,12
	19,15		18,14		17,13	16,12
	19,11		18,10		17,9	16,8
15,11	14,11	14,10	13,10	13,9	12,9	12,8
	11,11		10,10		9,9	8,8
	11,7		10,6		9,5	8,4
	7,7		6,6		5,5	4,4
	6,3		6,2		5,1	4,0
	3,3		2,2		1,1	0,0

243 linking continues until all mirrors in each side of RICH2 are related.
244 Consistent set of combinations is not unique. So we have chosen the set with maximal
245 populated combinations. That choice can be read off Fig. **??**.
246 Next we need a system of equations for finding these parameters. Each equation will
247 represent a combination of one primary and one secondary mirror segment. In reality,
248 the number of these equations hardly reaches the number of the unknowns, because
249 each mirror "collaborates" efficiently (in terms of reflecting the same photons) with not
250 more than a couple of other adjacent mirrors of the opposite kind. From the point of
251 view of geometrical optics, this means that a set of small rotations of one kind of mir-
252 rors can be approximately compensated by a set of small rotations of mirrors of the
253 opposite kind in the compensating directions, so that nothing changes on the photo-
254 detector plane. Therefore, a formally consistent system of 96 equations relating tilts
255 around y and z axes for 28 primary and 20 secondary mirrors will be ill-conditioned,
256 meaning that although there will always exist a formally unique solution, in practice it
257 will be unstable. That instability will reveal itself in non-convergence of the solutions,
258 because the magnification factors and the "measured" combined tilts for each combin-
259 ation will slightly variate from iteration to iteration, and although the system will be
260 numerically close to the previous one, it will yield a somewhat different solution which
261 will, in turn, result in a next fluctuation of the system, preventing further adjustments
262 from reaching desired smallness.
263 The most straightforward way to regularize the solution is simply to give up adjusting
264 one of the mirrors, fixing its adjustments to 0. We have chosen primary mirror 12 for
265 that. This is because of its relatively high photon population, being the closest mirror
266 to the beam pipe.
267 Among all possible mirror combinations we have consistently chosen first 47 combina-
268 tions from their list sorted according to their efficiency in jointly reflecting photons in
269 descending order. This choice is shown in Table 4 and Fig. 7.
270 As a result, we have a system of 94 linear equations (47 combinations of Equations 3).
271 We solve this system algebraically, by the substitution method at the combinations level
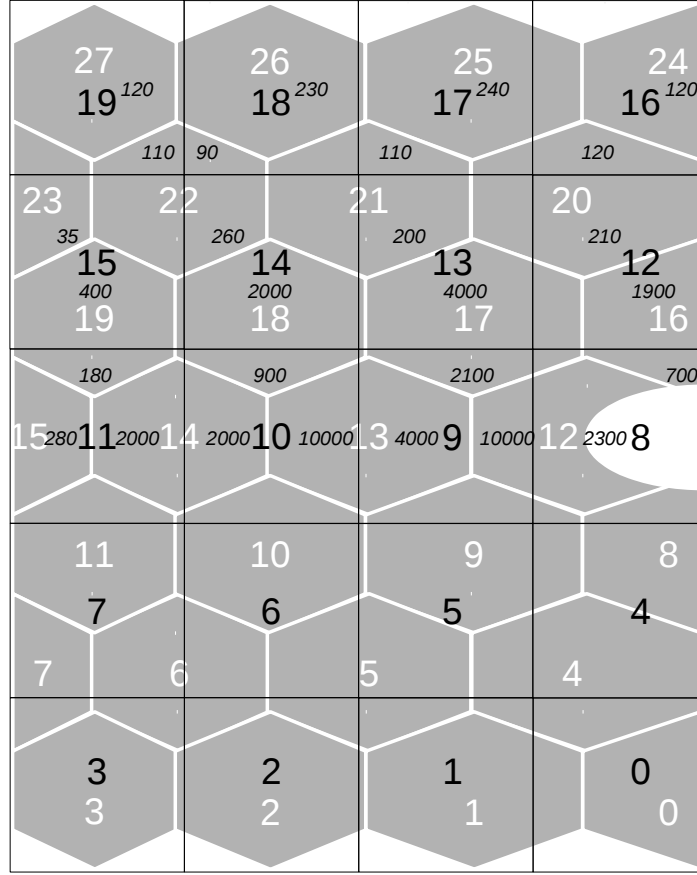
27 19 120   26 18 230   25 17 240   24 16 120

110 | 90   110   120

23   22   21   20

35   260   200   210

15   14   13   12

400   2000   4000   1900

19   18   17   16

180   900   2100   700

15 280 11 2000   14 2000 10 10000   13 4000 9 10000   12 2300 8

11   10   9   8

7   6   5   4

7   6   5   4

3   2   1   0

3   2   1   0

Figure 7: RICH2 (left-hand side) primary/secondary mirror optical overlapping and the optimal combining schema based on the results of the selection (Section **??**). Black transparent square boxes with black numbers – secondary mirrors, gray hexagons or trapezoids with white numbers – primary ones. The relative population numbers of the mirror combination histograms, taken from Fig. **??**, are multiplied by 10^4. The system of equations 3 follows this optimal overlapping schema.

(starting with setting tilts of primary mirror 12 equal to zero: $\alpha^y_{12} = \alpha^z_{12} = 0$) and with Cramer's rule — within each combination (system of equations 3).

Obviously, last paragraph of the previous section (Sec. 3.4.1) applies here too.

3.4.3 Improvement of the mathematical schema

The above approach to solving the system of equations for compensations for the individual mirror segment misalignments suffers from inequality: one mirror in each set of mirrors that are treated jointly, is privileged and is not being corrected at all. As it is pointed out above, this is because the whole geometrical configuration of the mirror system is inherently degenerate numerically.

In HERAb an attempt was implemented to solve the analogous system using least squares method augmented by requirement that the algebraic sum of the corrections

13

(secondary mirror adjustments are included with the opposite sign) is minimal, which gives them an additional equation that makes solution of the system quasi unique [12]. That system was solved by the weighted least squares method with two caveats: a) only dispersions of the right-hand sides were used and b) the weight for the squared discrepancy of the additional equation was chosen rather voluntarily. Although that approach eliminated privilege of one of the mirrors in each set, it is not satisfactory, and one of the reasons is that the additional equation is only a linear sum, while there should have been some sort of a quadratic sum.

We essentially improved the computations in the following way. Let us first consider general case and then translate the formulae to our specific notations. Let the underdetermined system of $n-1$ equations for n unknowns be

$$
\begin{array}{ccccccc}
a_{1,1}x_1 & +\cdots+ & a_{1,k}x_k & +\cdots+ & a_{1,n}x_n & = & b_1 \\
\vdots & \ddots & \vdots & \ddots & \vdots & & \vdots \\
a_{n-1,1}x_1 & +\cdots+ & a_{n-1,k}x_k & +\cdots+ & a_{n-1,n}x_n & = & b_{n-1}.
\end{array}
\tag{5}
$$

To get a unique solution we need, e.g., to determine one of the values, say x_k, a priori, from a different source. Simplest way is to fix it as $x_k = 0$.

Instead, we have chosen a more sophisticated method: we add a regularizing constraint. Namely, we minimize the overall perturbation of the system, i.e. minimize the Euclidean norm of the solution vector

$$
\sum_{j=1}^{n} x_j^2.
\tag{6}
$$

Then, modified "weighted" least squares method will consist in minimizing the following functional:

$$
\sum_{j=1}^{n} \left[\sum_{i=1}^{n-1} \frac{\left(b_i - \sum_{j=1}^{n} a_{i,j}x_j \right)^2}{\sigma^2(b_i) + \sum_{j=1}^{n} \sigma^2(a_{i,j})x_j^2} + x_j^2 \right],
\tag{7}
$$

.

while the in the "unweighted" case it becomes

$$
\sum_{j=1}^{n} \left[\sum_{i=1}^{n-1} \left(b_i - \sum_{j=1}^{n} a_{i,j}x_j \right)^2 + x_j^2 \right].
\tag{8}
$$

In our particular case and with our specific notations (this is equally valid for both RICH1 and RICH2), instead of (5) and (7), we have system of equations (9)

$$
\begin{array}{ccccc}
\vdots & \vdots & \vdots & \vdots & \vdots \\
A_{p,s}^y \alpha_p^y + B_{p,s}^y \beta_s^y + a_{p,s}^y \alpha_p^z + b_{p,s}^y \beta_s^z = \Theta_{p,s}^y \\
A_{p,s}^z \alpha_p^z + B_{p,s}^z \beta_s^z + a_{p,s}^z \alpha_p^y + b_{p,s}^z \beta_s^y = \Theta_{p,s}^z \\
\vdots & \vdots & \vdots & \vdots & \vdots
\end{array}
\tag{9}
$$

305 and we would minimize functional (10), respectively:

$$\sum_{p,s\in\text{subset}}\left[\frac{(\Theta^y_{p,s}-A^y_{p,s}\alpha^y_p-B^y_{p,s}\beta^y_s-a^y_{p,s}\alpha^z_p-b^y_{p,s}\beta^z_s)^2}{\sigma^2(\Theta^y_{p,s})+\sigma^2(A^y_{p,s})(\alpha^y_p)^2+\sigma^2(B^y_{p,s})(\beta^y_s)^2+\sigma^2(a^y_{p,s})(\alpha^z_p)^2+\sigma^2(b^y_{p,s})(\beta^z_s)^2}\right.$$

$$+\frac{(\Theta^z_{p,s}-A^z_{p,s}\alpha^z_p-B^z_{p,s}\beta^z_s-a^z_{p,s}\alpha^y_p-b^z_{p,s}\beta^y_s)^2}{\sigma^2(\Theta^z_{p,s})+\sigma^2(A^z_{p,s})(\alpha^z_p)^2+\sigma^2(B^z_{p,s})(\beta^z_s)^2+\sigma^2(a^z_{p,s})(\alpha^y_p)^2+\sigma^2(b^z_{p,s})(\beta^y_s)^2}\quad(10)$$

$$\left.+(\alpha^y_p)^2+(\alpha^z_p)^2+(\beta^y_s)^2+(\beta^z_s)^2\right].$$

306 For example, in the case of RICH2, (p,s) runs over the subset presented in Table 4 (or
307 its equivalent 5), plus the corresponding combinations of the right-hand side, that is
308 96 combinations from $0,0$ to $55,39$ with quite a number of omissions compared to the
309 straightforward set of all possible combinations on each side, which is 1120.
310 However, 10 is not the final functional yet. The traditional "weighted" sum is good
311 when the system is overdetermined and then the weights ensure that the influence of
312 the equations is proportional to the accuracy of their coefficients and of their right-hand
313 sides. In our case, we have carefully chosen a maximal set of mirror combinations that
314 gives underdetermined consistent system of equations. Weights would only distort the
315 solution, they are irrelevant and even harmful in our case, and so the functional (the 8
316 type) becomes

$$\sum_{p,s\in\text{subset}}\left[(\Theta^y_{p,s}-A^y_{p,s}\alpha^y_p-B^y_{p,s}\beta^y_s-a^y_{p,s}\alpha^z_p-b^y_{p,s}\beta^z_s)^2\right.$$

$$+(\Theta^z_{p,s}-A^z_{p,s}\alpha^z_p-B^z_{p,s}\beta^z_s-a^z_{p,s}\alpha^y_p-b^z_{p,s}\beta^y_s)^2\quad(11)$$

$$\left.+(\alpha^y_p)^2+(\alpha^z_p)^2+(\beta^y_s)^2+(\beta^z_s)^2\right].$$

317 A "weighted" solution with minimization of just linear sum of the solution vector ele-
318 ments was used in HERAb [8] while "weighted" without regularization was used in
319 earlier LHCb publication [6].
320 Moreover, the regularization can be made more efficient, taking advantage of the fact,
321 that the magnification factors belonging to each family, are close to the respective av-
322 erage. While the average minor magnification factors $\overline{a^y}$, $\overline{a^z}$, $\overline{b^y}$, and $\overline{b^z}$ are quite small,
323 and therefore can be neglected in the context of the regularization term, the major ones
324 are significant and distinctly different (see Table 6).
325 We can then upgrade the regularization term of 11 by multiplying the solution compon-
326 ents by the respective average major magnification factors, and the final form of the
327 functional is:

$$\sum_{p,s\in\text{subset}}\left[(\Theta^y_{p,s}-A^y_{p,s}\alpha^y_p-B^y_{p,s}\beta^y_s-a^y_{p,s}\alpha^z_p-b^y_{p,s}\beta^z_s)^2\right.$$

$$+(\Theta^z_{p,s}-A^z_{p,s}\alpha^z_p-B^z_{p,s}\beta^z_s-a^z_{p,s}\alpha^y_p-b^z_{p,s}\beta^y_s)^2\quad(12)$$

$$\left.+(\overline{A^y}\alpha^y_p)^2+(\overline{A^z}\alpha^z_p)^2+(\overline{B^y}\beta^y_s)^2+(\overline{B^z}\beta^z_s)^2\right].$$

Table 6: Average major magnification factors.

		RICH1	RICH2
primary mirrors	$\overline{A^y}$	1.86	2.05
	$\overline{A^z}$	2.02	1.83
secondary mirrors	$\overline{B^y}$	−0.55	−1.04
	$\overline{B^z}$	0.81	0.61

The final functional 12 treats the solution components in a more "fair" way, in accordance with their "influence strength". Therefore, at every iteration, its minimization potentially yields a solution that is closer to final solution, and hence may reduce the number of iterations.

4 The Online Alignment Framework

4.1 Dataflow in Run II

The LHCb trigger strategies for the Run I and Run II data taking periods are shown in Figure 8.
In Run I the online event reconstruction was simpler and faster than the reconstruction used offline and did not include any information about the particle identification (PID). In order to have the same reconstruction online and offline as well as using the PID information in the HLT2 the data-taking strategy has been amended for Run II. As in Run I a rate of $1\,\mathrm{MHz}$ of events passes the level-0 trigger (L0) and is passed on to the first high level trigger stage (HLT1). There the events are partially reconstructed and accepted events are written to disk. At this stage the different alignments are run on a dedicated part of the buffered data. In case of a big shift in alignment constants the new constants are propagated to the LHCb conditions database and used in the subsequent processing of the events by the second high level trigger (HLT2).
The alignment tasks being performed on the data are - in the order they are being run - VELO alignment, tracker alignment, RICH alignment and finally muon chamber alignment. Each alignment has its own dedicated HLT1 line which collects a given number of events at the beginning of each fill (see Section 4.2 for the RICH lines). It has been found that ∼1 M events for RICH1 and ∼2 M events for RICH2 is sufficient to produce stable results. Once enough events have been collected the alignment is started.

4.2 HLT1 selection for the RICH mirror alignment

In order to determine the misalignments on the detector plane and subsequently the individual mirror misalignments the $\delta\theta$ vs. ϕ histograms for each mirror combination have to contain enough entries for the fits described in Section 3.3 to converge. The minimum condition for a successful fit has been found to be that 16 of the 20 bins in ϕ
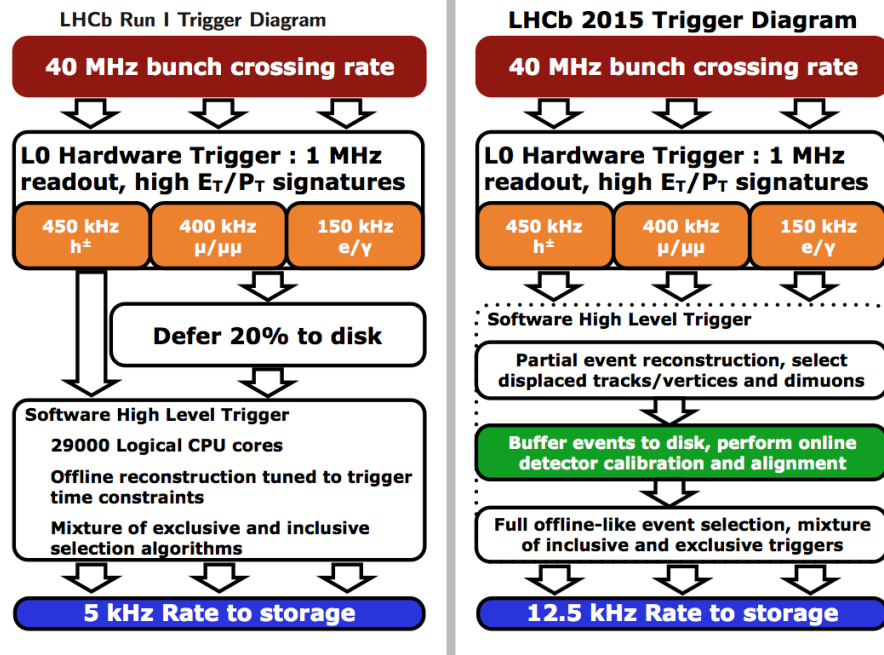
16

Figure 8: LHCb dataflow for Run I (left) and Run II (right). In Run II the data is buffered after HLT1 and an alignment is performed for each fill. The HLT2 will then process the buffered events with the updated alignment constants.

358 have to contain at least 300 entries.
359 This is accomplished by having two dedicated HLT1 selections, one each for RICH1
360 and RICH2. The lines trigger on high energy particle tracks whose Cherenkov photons
361 would populate the mirror combinations containing the fewest photons. The other mir-
362 ror combinations are then populated by the rest of the tracks in the events.
363 The variables used in the selection are the track momentum p, the transverse track
364 momentum p_T, the pseudorapidity η, the goodness of fit for the track χ^2 and the polar
365 angle of the track ϕ. The selection criteria of tracks that are triggered upon are listed
366 in Table 7.

Table 7: Trigger criteria for the HLT1 line for RICH1 and RICH2. Events that are accepted by these trigger lines need to have at least one track that satisfies the cuts listed below.

	RICH1	RICH2
momentum p	$p > 20$ GeV	$p > 40$ GeV
transverse momentum p_T	$p_T > 0.5$ GeV	$p_T > 0.5$ GeV
pseudorapidity η	$1.6 < \eta < 2.04$	$2.65 < \eta < 2.80$
track χ^2	$\chi^2 < 2$	$\chi^2 < 2$
polar angle Φ	$-2.65 < \Phi < -2.30$	$-2.59 < \Phi < -2.49$
	$-0.80 < \Phi < -0.50$	$-0.65 < \Phi < -0.55$
	$0.50 < \Phi < 0.80$	$0.55 < \Phi < 0.65$
	$2.30 < \Phi < 2.65$	$2.49 < \Phi < 2.59$

17

4.3 The Alignment Farm

All alignments are run on the alignment farm. The alignment farm consists of approximately 1700 CPUs, called *analysers* and a central node called the *iterator*.
The data taken from the HLT1 selection for the RICH alignments is stored evenly distributed over the analysers until it can be processed by HLT2. The analysers perform the event reconstruction with a database provided to them by the iterator and fill the $\delta\theta$ vs. ϕ histograms mentioned in Section 3. Apart from providing the database with the desired mirror orientations the iterator also performs the fits on the histograms, determines the individual mirror misalignments, produces a new database and decides whether the alignment procedure has converged or whether another iteration has to be performed. If the latter is the case, the iterator will make the new database available to the analysers (for more details see Section 4.5).
The advantage of having a system consisting of about 1700 nodes distributed over 50 farms is that the event reconstruction can happen in parallel and is therefore very fast. This parallel processing is asynchronous and has to be coordinated between the individual analysers and the iterator which is described in the next section.

4.4 The Control Flow

The execution of the alignment tasks is under the control of the LHCb Experiment Control System (ECS), and is implemented as a *finite state machine*, which is illustrated in Figure 9. The principle of a finite state machine means that each component of the system (here every individual analyser and the iterator) has to be in one of a finite number of states at all times. The states used for the alignment procedure are also shown in Figure 9, such as "READY", "RUNNING" and "PAUSED". The alignment is then steered by the *run control* that can see all the components and their individual states and can send commands. Those commands will be received by the individual components and they will act accordingly. For a given state only a certain number of commands are possible - for example if the component is in state "PAUSED" it can only receive the commands "continue" and "stop". If a command is received the component will go from its state into the state declared by Figure 9. When in a new state the component will usually perform a task and then set itself into another state once finished so that the run control is aware of this task being completed.

4.5 Implementation of the RICH Mirror Alignment for Run II

The interplay between the iterator, one example analyser and the run control during the course of the alignment of a RICH detector is shown in Figure 10.
The individual analysers and the iterator all follow the same sequence of states, namely the one shown in Figure 9. When the alignment is being started the run control sends the command to "configure" to both the iterator and all analysers. All components will go into state "CONFIGURING" while setting up to run the alignment. For the analysers this means that they read in the configuration for the reconstruction of the
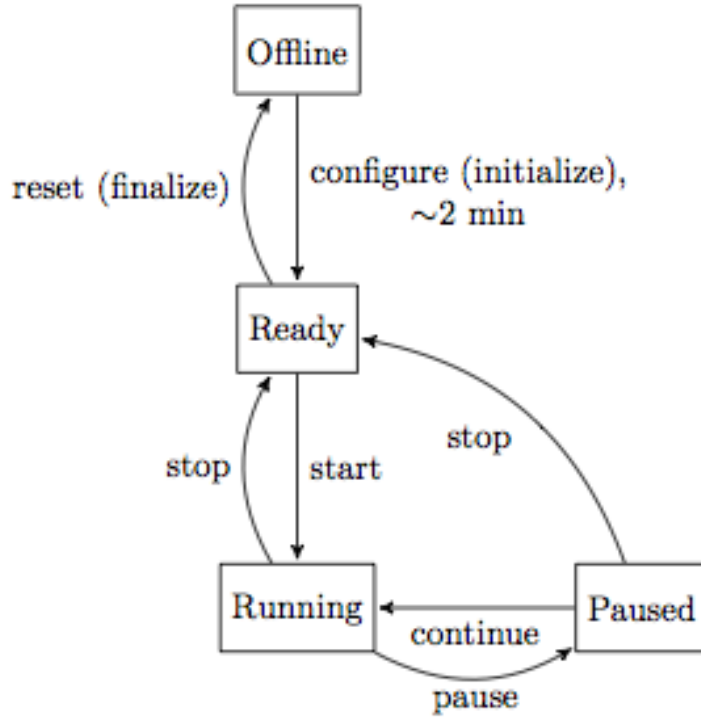
Figure 9: Example of one component within a system functioning under the principle of a finite state machine. The boxes show the states the component is in while the arrows show the commands the component gets from the run control.

events, while the iterator sets up a directory in which all files for this alignment are saved.

Each component goes into state "READY" when it is done configuring. When all tasks are in the "READY" state, the iterator makes an initial set of alignment constants available to the analysers and then updates its state to "RUNNING". The analyzers are then sent the "start" command, update their state to "RUNNING" and start reconstructing the data stored on them. Each analyser that has completed processing its data updates its state to "PAUSED", and once they have all reached this state, the run control sends the stop command and they update their states to "READY". The iterator is then sent the "pause" command, collects and combines the histograms produced by the analyser tasks and performs the fits. It then calculates the individual mirror misalignments and produces a new database containing the mirror orientations. The it either indicates that conversion has been reached by updating its state to "READY", or that further iteration is required by updating its state "RUNNING". In the latter case the iterator will provide the new database to the analysers before changing its state and another iteration is started.
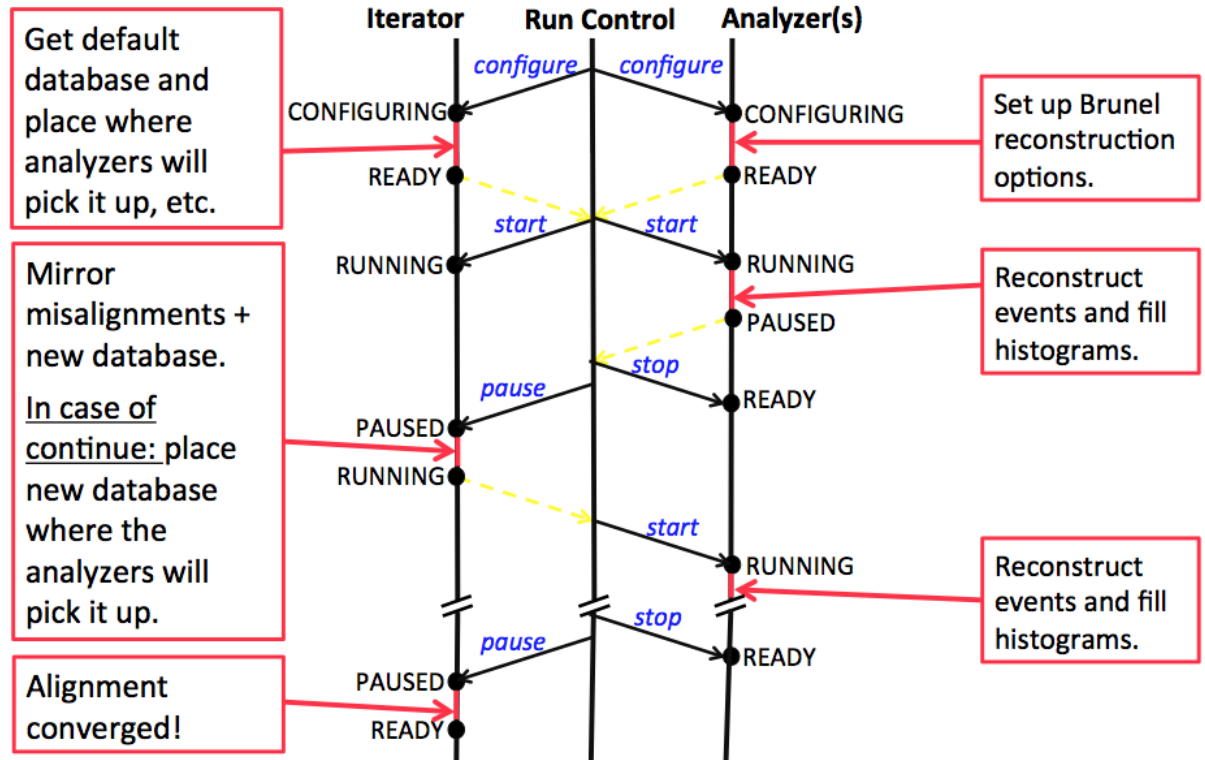
19

Figure 10: Interplay between the iterator, one example analyser and the run control during the RICH alignment procedure. The analysers reconstruct the data and produce the histograms that the iterator evaluates. The run control makes sends commands to the iterator and the analysers to make sure the alignment procedure happens in the necessary sequence.

References

[1] LHCb collaboration, A. A. Alves Jr. *et al.*, *The LHCb detector at the LHC*, JINST **3** (2008) S08005.

[2] M. Adinolfi *et al.*, *Performance of the LHCb RICH detector at the LHC*, Eur. Phys. J. **C73** (2013) 2431, arXiv:1211.6759.

[3] LHCb collaboration, R. Aaij *et al.*, *LHCb detector performance*, Int. J. Mod. Phys. **A30** (2015) 1530022, arXiv:1412.6352.

[4] LHCb Collaboration, *LHCb RICH technical design report*, CERN-LHCC-2000-037.

[5] LHCb Collaboration, *LHCb technical design report: reoptimized detector design and performance*, CERN-LHCC-2003-030.

[6] A. Papanestis, *The calibration and alignment of the LHCb RICH system*, Nucl. Instrum. Meth. **A595** (2008) 248.

[7] W. Baldini *et al.*, *LHCb alignment strategy*, LHCB-2006-035.

[8] A. Gorisek, P. Krizan, S. Korpar, and M. Staric, *Alignment of the HERA-B RICH optical system with data*, Nucl. Instrum. Meth. **A433** (1999) 408.

[9] I. Arino *et al.*, *The HERA-B ring imaging Cherenkov counter*, Nucl. Instrum. Meth. **A516** (2004) 445.

[10] I. Antcheva *et al.*, *ROOT: A C++ framework for petabyte data storage, statistical analysis and visualization*, Comput. Phys. Commun. **182** (2011) 1384.

[11] C. D'Ambrosio, L. Fernndez, M. Laub, and D. Piedigrossi, *The optical systems of LHCb RICHes: a study on the mirror walls and mirrors specifications*, LHCb-2000-071.

[12] M. Staric and P. Krizan, *Calibration of the mirror system in the HERA-B RICH*, Nucl. Instrum. Meth. **A586** (2008) 174.